

Remote Monitoring of Subsurface Flow Conditions in Rivers

Christopher J. Zappa
Lamont-Doherty Earth Observatory of Columbia University
Ocean and Climate Physics Division
61 Route 9W
Palisades, NY 10964
Phone: (845) 365-8547 fax: (845) 365-8157 email: zappa@ldeo.columbia.edu

Award Number : N00014-11-1-0168

LONG-TERM GOALS

The primary research goal is to develop techniques to determine subsurface turbulence from remote measurements using infrared imaging of the skin layer. We aim to infer flow rate, turbulence intensity and subsurface-generated turbulent structures from surface temperature patterns. We will take advantage of the two complementary indicators of subsurface flow provided by IR imagery: the thermal structures measured directly and the surface velocity fields obtained through various image processing techniques. We will (1) analyze the variability and structures of the thermal boundary layer, (2) compute the surface flow field from the IR imagery and infer further surface turbulence characteristics, (3) determine to which extent the turbulence in the boundary layer is due to surface forcing by analysis of the air-sea flux data and (4) determine empirical relationships of subsurface flow characteristics and of turbulence derived from in situ sub-surface data to the observed turbulence in the IR imagery. We further aim to determine the limits of remotely inferring flow rates, subsurface turbulence and bed stress from IR imagery. We will investigate how different wind, tides and wave breaking conditions affect our ability to remotely measure subsurface flow characteristics.

OBJECTIVES

The skin temperature is governed by surface and subsurface processes. Net air-water heat flux leads to a cooler thermal boundary layer (TBL) compared to the underlying bulk layer. Turbulent motions resulting from wind forcing at the air-sea interface and from turbulent eddies generated within the water column, disrupt the TBL, mixing it with the bulk layer. During the last century links between air-water transfer and bulk turbulence were researched (*Brumley and Jirka*, 1988; *Danckwerts*, 1951). Only in the last decade, has the TBL been recognized as the intermediate step between subsurface turbulence and air-water transfer and as such was used as a more direct indicator for air-water transfer (*McKenna and McGillis*, 2004). This study will use the TBL as a direct indicator for subsurface turbulence and provide predictive relationships of the surface-bulk connection. It will result in a set of universal curves connecting remotely collected surface measurements to fundamental local flow quantities – the flow depth, the bed stress, the bulk mean flow and the bulk turbulent kinetic energy.

Report Documentation Page				Form Approved OMB No. 0704-0188	
Public reporting burden for the collection of information is estimated to average 1 hour per response, including the time for reviewing instructions, searching existing data sources, gathering and maintaining the data needed, and completing and reviewing the collection of information. Send comments regarding this burden estimate or any other aspect of this collection of information, including suggestions for reducing this burden, to Washington Headquarters Services, Directorate for Information Operations and Reports, 1215 Jefferson Davis Highway, Suite 1204, Arlington VA 22202-4302. Respondents should be aware that notwithstanding any other provision of law, no person shall be subject to a penalty for failing to comply with a collection of information if it does not display a currently valid OMB control number.					
1. REPORT DATE 2012		2. REPORT TYPE N/A		3. DATES COVERED -	
4. TITLE AND SUBTITLE Remote Monitoring of Subsurface Flow Conditions in Rivers				5a. CONTRACT NUMBER	
				5b. GRANT NUMBER	
				5c. PROGRAM ELEMENT NUMBER	
6. AUTHOR(S)				5d. PROJECT NUMBER	
				5e. TASK NUMBER	
				5f. WORK UNIT NUMBER	
7. PERFORMING ORGANIZATION NAME(S) AND ADDRESS(ES) Lamont-Doherty Earth Observatory of Columbia University Ocean and Climate Physics Division 61 Route 9W Palisades, NY 10964				8. PERFORMING ORGANIZATION REPORT NUMBER	
9. SPONSORING/MONITORING AGENCY NAME(S) AND ADDRESS(ES)				10. SPONSOR/MONITOR'S ACRONYM(S)	
				11. SPONSOR/MONITOR'S REPORT NUMBER(S)	
12. DISTRIBUTION/AVAILABILITY STATEMENT Approved for public release, distribution unlimited					
13. SUPPLEMENTARY NOTES The original document contains color images.					
14. ABSTRACT					
15. SUBJECT TERMS					
16. SECURITY CLASSIFICATION OF:			17. LIMITATION OF ABSTRACT SAR	18. NUMBER OF PAGES 16	19a. NAME OF RESPONSIBLE PERSON
a. REPORT unclassified	b. ABSTRACT unclassified	c. THIS PAGE unclassified			

APPROACH

Building on our extensive expertise in IR imagery and our experience in making near-boundary turbulence measurements, we aim to determine empirical relationships between surface length-scales and flow and sub-surface flow and turbulence. During the prototype field campaign, data was collected with the following instruments:

- IR camera: a Cedip Jade III longwave camera was mounted a pan/tilt system from the A-frame of a moored ship. This set up allowed us to move the camera with the current so to always view upstream of the ship. The Cedip Jade III offers better than 15 mK temperature resolution, with 200 Hz max frame rate, 14-bit digitization, and 320 x 240 pixels. The sampling frequency was set to 60 Hz.
- Air-Sea Flux package: a meteorological station was mounted on a piling neighbouring the ship to get measurements of wind speed & direction, relative humidity, atmospheric pressure, air temperature, solar insolation, and longwave radiation.
- Acoustic Doppler Velocimeter (ADV): a Nortek Vector type ADV was mounted on the aforementioned piling at 11m above the River bed. Data was collected in 10 min bursts at top of every ½ hr, with a sampling frequency 32Hz.
- Higher Resolution Profilers: 2 Nortek Aquadopp were mounted on the piling at 3 and 6 m above the river bed. They offer a 1-cm resolution. Data was collected in 59.9 min burst at top of every hour, with a sampling frequency 2 Hz.
- CTDs: 3 CTDs were mounted on the piling at the same levels as the ADV and Aquadopps

The team's envisaged data analysis effort includes: image processing and analysis of the IR imagery to characterize surface turbulence. This comprises calculation of the statistical moments, histograms to assess surface skin temperature variability, and determination of length scales of the skin temperature structures. Further 3 methods to determine the surface velocity field from the IR imagery will allow inferring integral length scales, as well as the surface turbulent kinetic energy and calculation of divergence. The bulk Reynolds number can then be determined from the divergence. Analysis of the Aquadopps, ADV and CTD data combined will provide a robust measure of subsurface turbulent, convective, and advective motions. Links between the subsurface and surface turbulence will be investigated, keeping in mind that the observed turbulence at the surface is partly due to surface forcing. Processing and analysis of the direct measurement of heat, mass and momentum fluxes across the air-water interface along with measurements of the radiative forcing will permit to separate the different processes (wind-driven, bed-driven, buoyancy-driven, and convective) which lead to surface turbulence.

WORK COMPLETED

Our efforts in FY11 comprised image processing and analysis of the IR imagery taken from the ship so to determining the temperature variability and scales of observed patterns. Further the 3 methods to determine the surface flow were applied and compared to one another as well as to in-situ ADV data.

RESULTS

The field campaign was undertaken in the Hudson River on the nights of November 18th and 19th 2010. The study area, shown in Figure 1 (left), 20 miles north of Manhattan, is located by the State Line Lookout in the Palisades Interstate Park, NJ. A series of 10 minute surface IR measurements were taken simultaneously from the top of the State Line Lookout cliff (camera deployed by Dugan's team) and from a boat. Throughout the campaign, the boat was moored within the field of view of the cliff top camera. IR data were collected every 30 minutes between 0100-0600 UTC on the 18th (yearday 322) and between 0400-1000 UTC on the 19th (yearday 323) amounting to a total of 23 runs. Surface and subsurface in situ instruments mounted on a piling, as shown in Figure 1 (right), provided measurements of environmental parameters such as wind speed, heat fluxes, air and water temperatures, humidity as well as subsurface currents, turbulence and salinity.

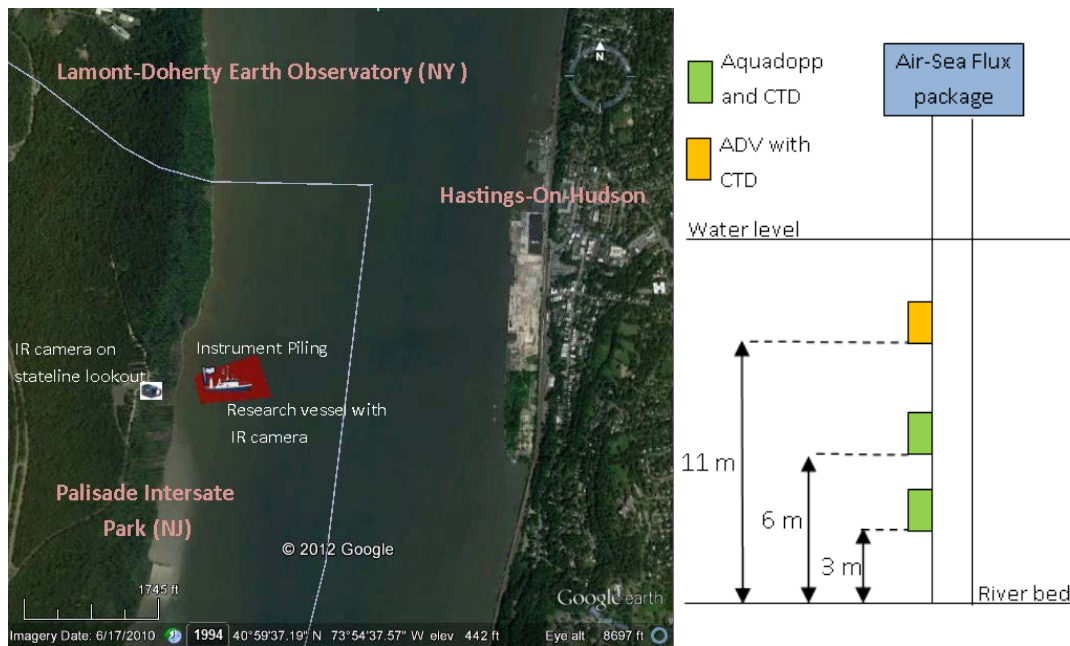


Figure 1. The left panel shows a Google Earth satellite image of the study area. The red polygon represents the field of view the IR camera mounted on the Cliff of the State line Lookout, within which the boat and the instrument piling were located. The right panel shows a schematic of the in situ instruments deployed

Environmental conditions

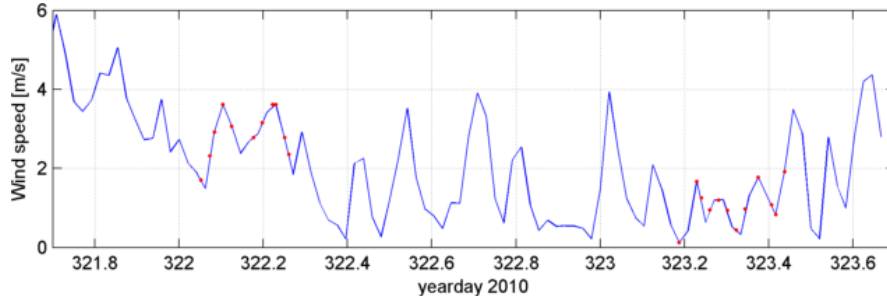


Figure 2. Time series of the 30 minute averaged horizontal wind magnitude measured by the meteorological station, the red dots represents the IR data collection periods

During the prototype field campaign IR measurements were taken under varying wind conditions as shown in Figure 2. The wind was stronger on the night of the 18th (yearday 322) than on the night of the 19th (yearday 323). The 30 minute maximum wind speed ranged from 0.12 m s⁻¹ to 3.62 m s⁻¹.

Time series of the net, the sensible and the latent heat flux as well as of the long and shortwave radiation and momentum flux (stress) for every 30 minutes are shown in Figure 3. The net heat flux (Q_{net}) on the night of the 18th was of -139.95 ± 23.21 W/m², whereas on the night of the 19th it was of -145.43 ± 63.78 W/m². As the field campaign took place during the night-time, the shortwave radiation was equally small during both nights. The net longwave radiation which includes the downward longwaves measured by the meteorological station and the upward longwave radiation from the sea surface ($\sim \epsilon \sigma SST^4$) was of -81.46 ± 25.88 W/m² on the first night and -89 ± 31.67 W/m² on the second night. The sensible heat flux was mostly positive on the 18th ($+10.52 \pm 12.04$ W/m²), but negative on the 19th (-12.89 ± 14.88 W/m²) and a generally stronger latent heat flux was recorded on 18th -66.65 ± 22.07 W/m² compared to -41.16 ± 34.68 W/m² 19th. The momentum flux was much stronger on the 18th with a mean and standard deviation of 0.30 ± 0.23 kg/m s²; on the 19th it only reached 0.125 ± 0.08 kg/m s².

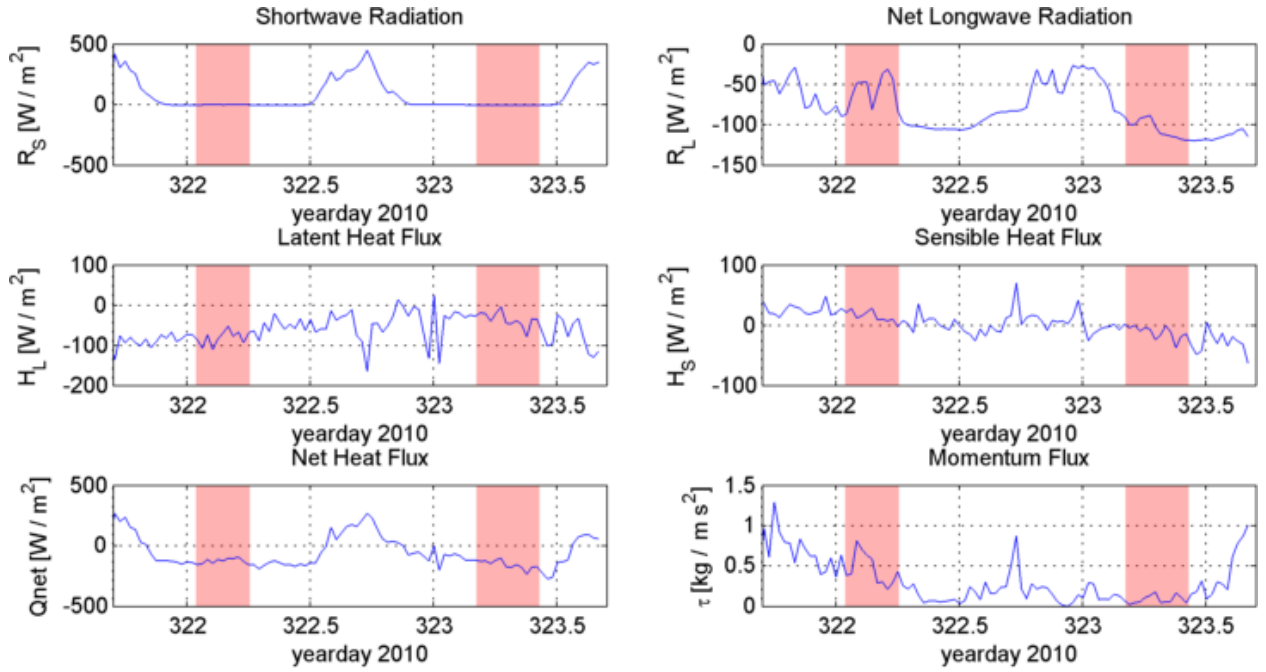


Figure 3. Time series of the shortwave and net longwave radiation, the latent, sensible and net heat fluxes as well as of the momentum flux (stress) measured by the meteorological station. The shading represents the IR data collection periods

Skin temperature variability

The IR imagery shows high variability in small-scale structures. Figures 4-7 show examples of the different patterns observed, which range from along-wind elongated streaks to more rounded boils. Breaking is clearly visible under the high wind conditions that prevailed during the night of the 18th as can be seen in Figure 4 & 5. Elongated streaks are mostly present under stronger winds, when no waves and breakers are present as exemplified in Figure 6. Whereas under very low wind conditions, we mostly observed boils and more sinuous streaks as seen in Figure 7.

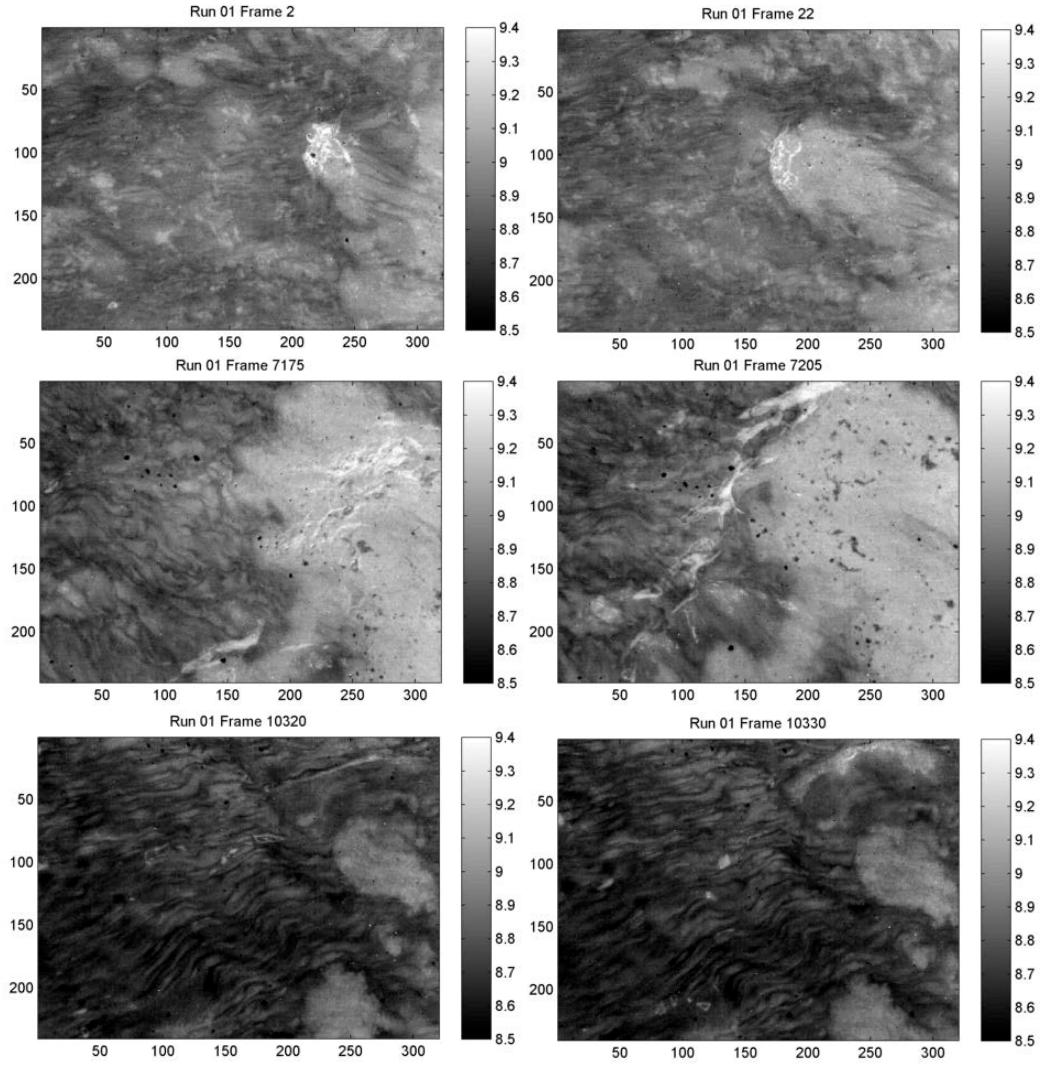


Figure 4. Breakers and temperature structures under high wind conditions during run 1 on the 18th ($|U| \sim 1.7\text{m/s}$)

Under strong winds, reflections overlay the temperature signature in the IR imagery, such as in Figure 5. These are not easily detectable on still images, but when a sequence of images is displayed as a movie, one can easily detect the skin temperature underlying the reflection which appears as a semi-transparent film. We are working on developing a robust method to filter out the reflective signal. More to the proposed method will be found in the last section.

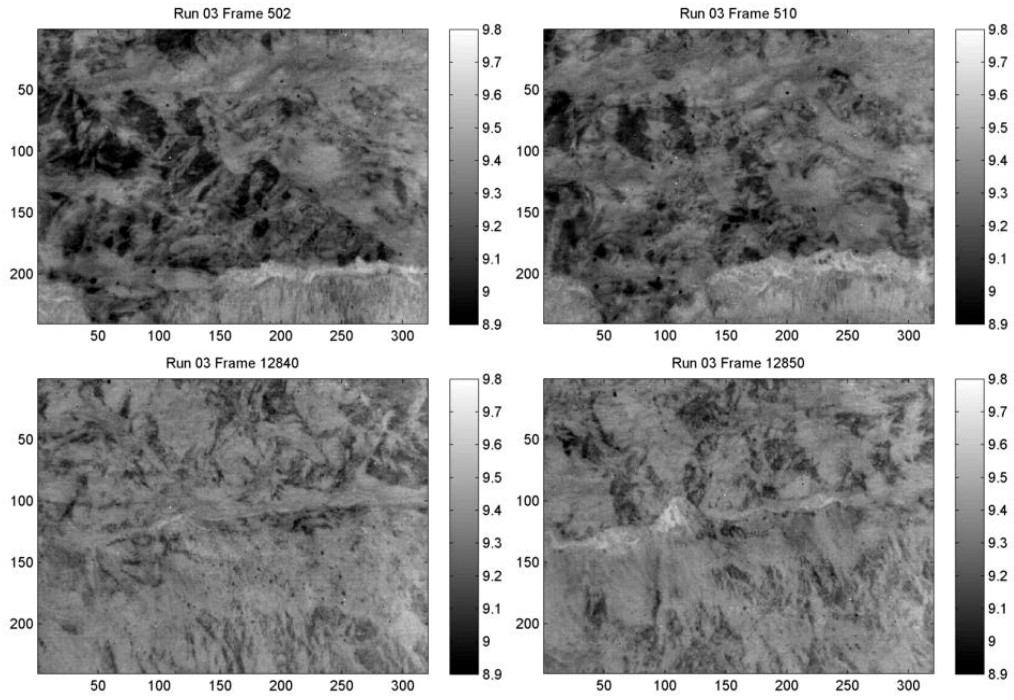


Figure 5. Waves passing through during run 3 on the 18th ($|U| \sim 2.9 \text{ m/s}$).

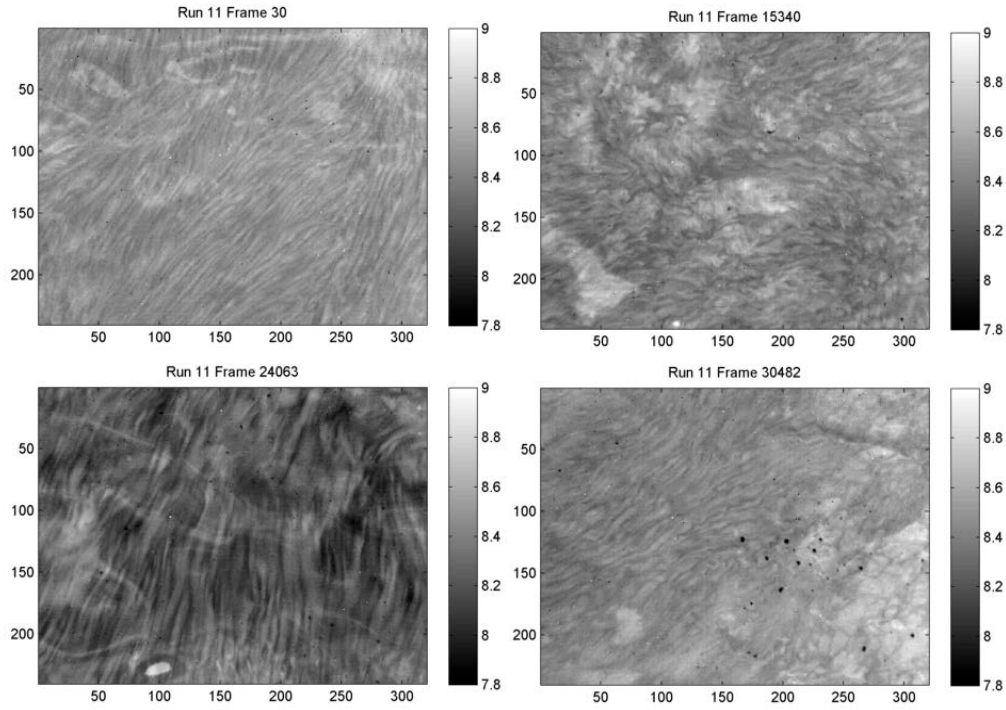


Figure 6. Skin temperature structures under calmer wind conditions during run 11 on the 18th ($|U| \sim 2.36 \text{ m/s}$).

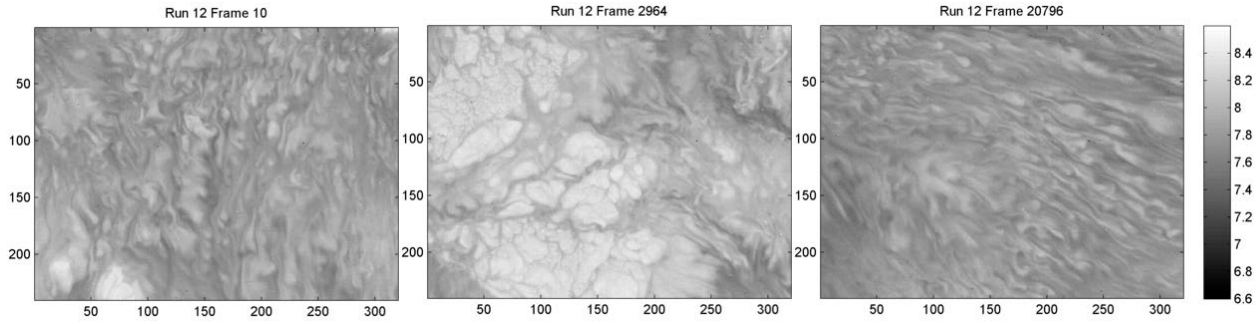


Figure 7. Skin temperature structures under calmer wind conditions during run 12, the first run on the 19th.

Figure 8 below illustrates the different types of temperature distributions observed during each run. Each histogram corresponds to the skin temperature of a whole run, i.e. over 10 min. Most runs have a distribution resembling that suggested by *Garbe et al.* [2003] as exemplified by the histogram of run 03. However, there are also distributions skewed the opposite way and Gaussian-looking histograms as for run01 and run11 respectively. Run12 displays a clearly bimodal histogram. The different distributions arise from the fact that over 10 minutes the skin temperature varies quite substantially and that hence looking at run means does not provide an adequate way to characterize the distribution of the skin temperature. Indeed, as shown in Figure 9, the frame mean temperature is not constant over the duration of a run. It can vary by 0.3 °C or more.

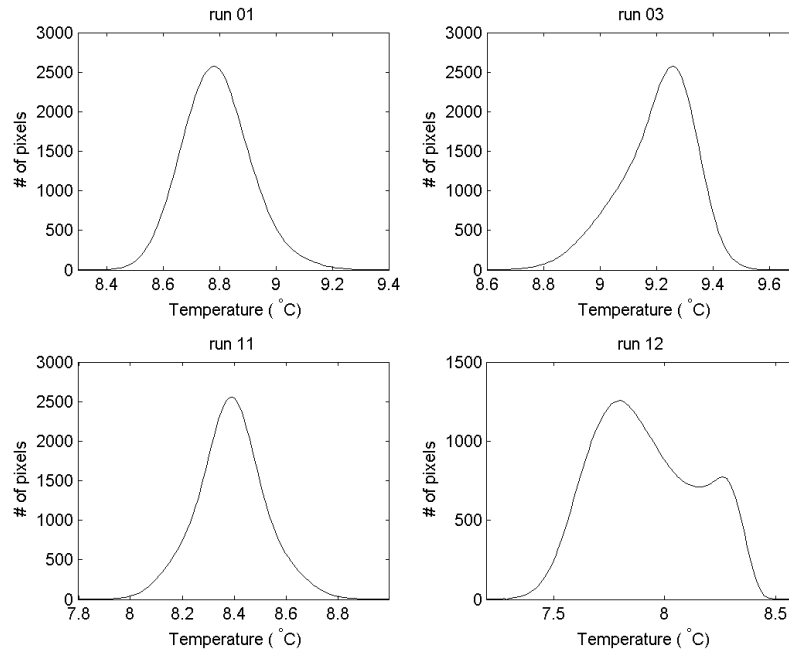


Figure 8. Histograms of the skin temperature distribution over 10 minutes for run 01, 03, 11 and 12.

However, high variability may also be observed within an individual frame. The right panel of Figure 9 shows time series of the standard deviation of the skin temperature per per frame. It is clearly visible that the standard deviations are higher for run 12 than for the other runs. This suggests that the bimodal distribution seen in Figure 8, may be due to bimodal variability within a frame rather than over the run. Computing a histogram for each frame and plotting them as a 2D time series as shown in Figure 10, lifts the doubt as bimodal distributions are clearly visible for most frames of run12, unlike for the other runs.

Run 12 was recorded under the calmest wind conditions compared to runs 1, 3 and 11. The high observed spatial skin temperature variability can be explained by the fact that the weaker wind less effectively mixes the surface, mixing water up at a lower rate. Stronger winds generate more mixing and can hence lead to a more uniform skin temperature distribution.

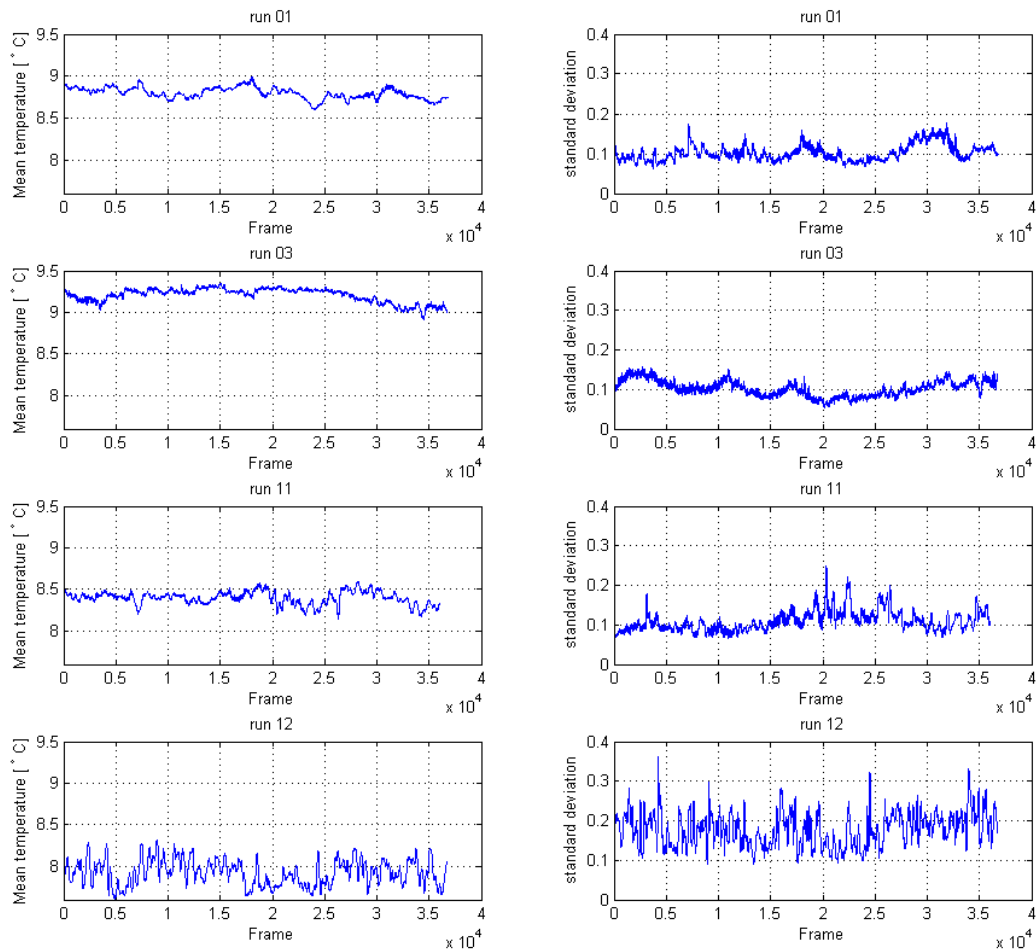


Figure 9. Timeseries of the frame mean temperature (left) and standard deviation (right) for runs 01, 03, 11 and 12.

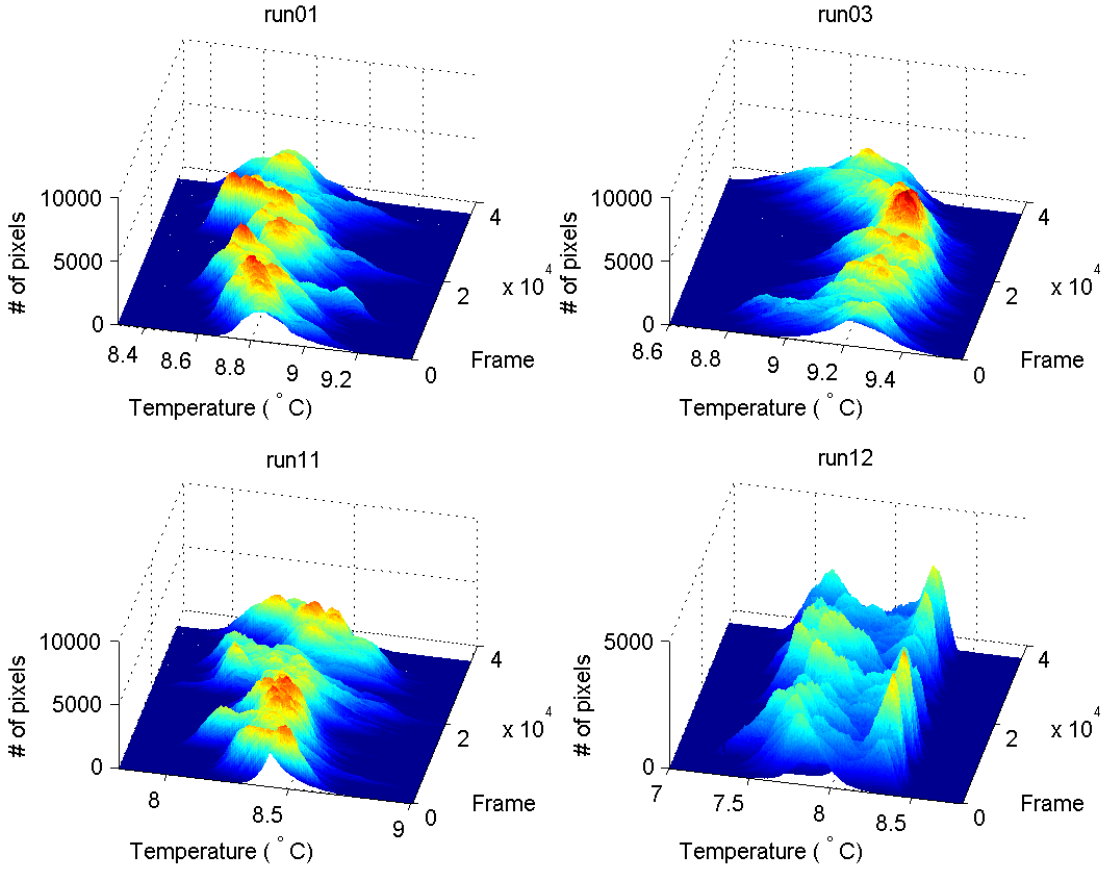


Figure 10. Time series of frame skin temperature histograms for runs 01, 03, 11 and 12.

Scale analysis of Skin Temperature

Calculating the normalized autocorrelation function for each row and column of a frame and then averaging over the rows and column to get frame mean normalized autocorrelation function allows inferring the length scale, in the x and y direction, of the surface skin patterns. The length scale is taken as the lag at which the normalized autocorrelation function goes to zero.

Figure 11a shows an example of a time series of frame mean normalized autocorrelation function from which the integral length scales are calculated. The integral length scales vary quite substantially over the length of a run as can be seen in Figure 11b. As expected the calculated length scales are more anisotropic under high wind conditions. The integral length scales calculated vary between 30.30 ± 12.53 pixels and 70.02 ± 26.75 pixels, with 1 pixel approximately equal to 1cm. Our ongoing analysis includes linking the length scales and associated viabilities to measured surface forcing and sub-surface turbulence.

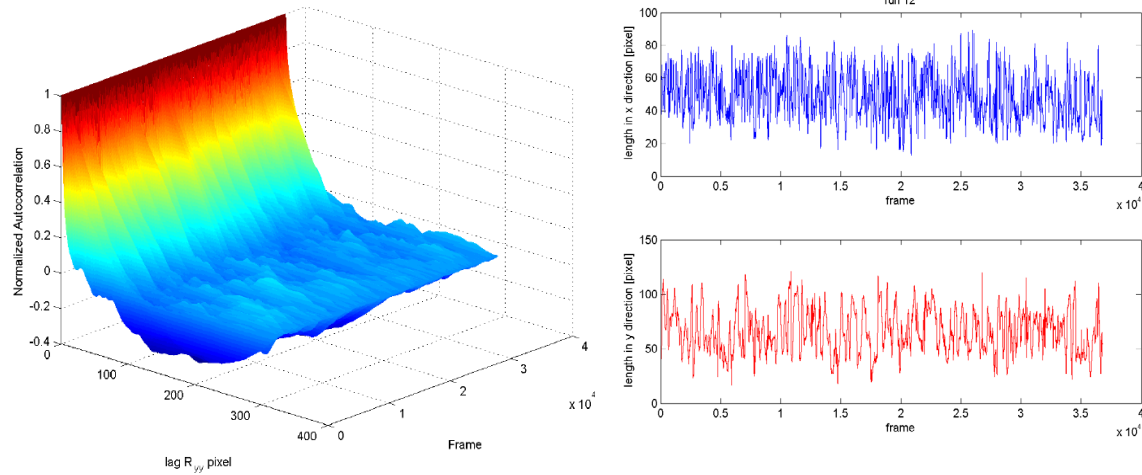


Figure 11-Time series showing an example of (left) the normalized auto correlation function in the y direction relative to the image, (right) of the calculated integral length scales in the x and y direction for run 12.

Surface Flow from IR imagery

Surface velocity fields have been determined by 3 approaches:

- Feature tracking or PIV
- Optical flow (OF)
- From advective surface in 3D spectra of the skin temperature (SAS)

The feature tracking PIV method is based on 2D spatial correlations between 16 x 16 pixels correlation windows in a first frame and 32 x 32 pixel search window in a second image. The two frames are consecutive, taken at a rate of 60 Hz. Velocities are determined on nodes spaces 8 pixels apart in the x and y direction. Figure 12, shows an example of the PIV, where a breaker is clearly visible.

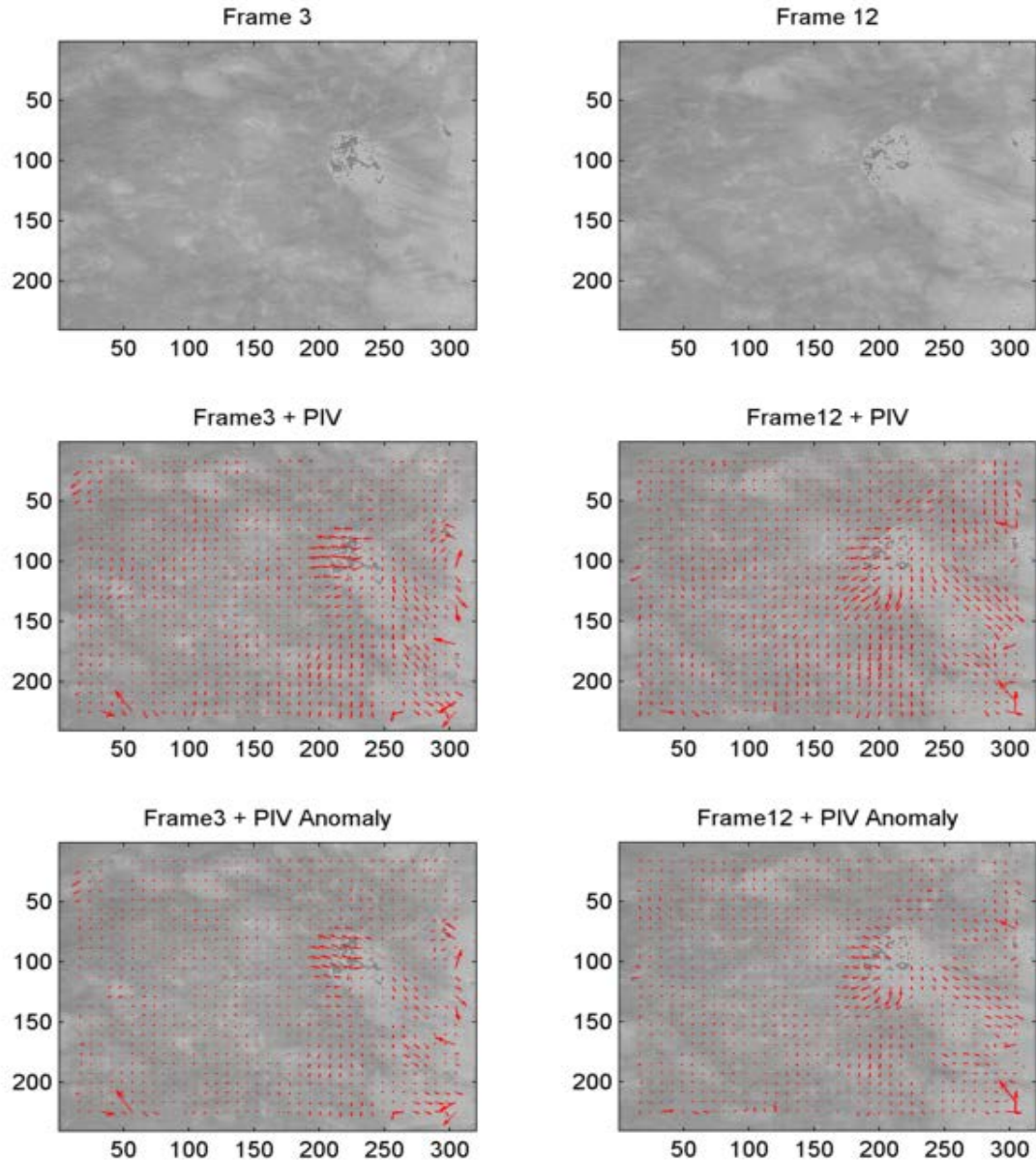


Figure 12- example of the PIV derived velocity field for two frames 3/20s apart during run 1.

The OF algorithm used is based on the Lukas-Kanade (LK) method that assumes a constant flow field throughout a burst of images and approximates the displacement from the changed in image intensity. The partial spatial derivatives of the differential algorithm are calculated with the Fourier Transform of the images and a flow vector is obtained for every pixel. Figure 13. shows an example of the OF for the same two frames shown above.

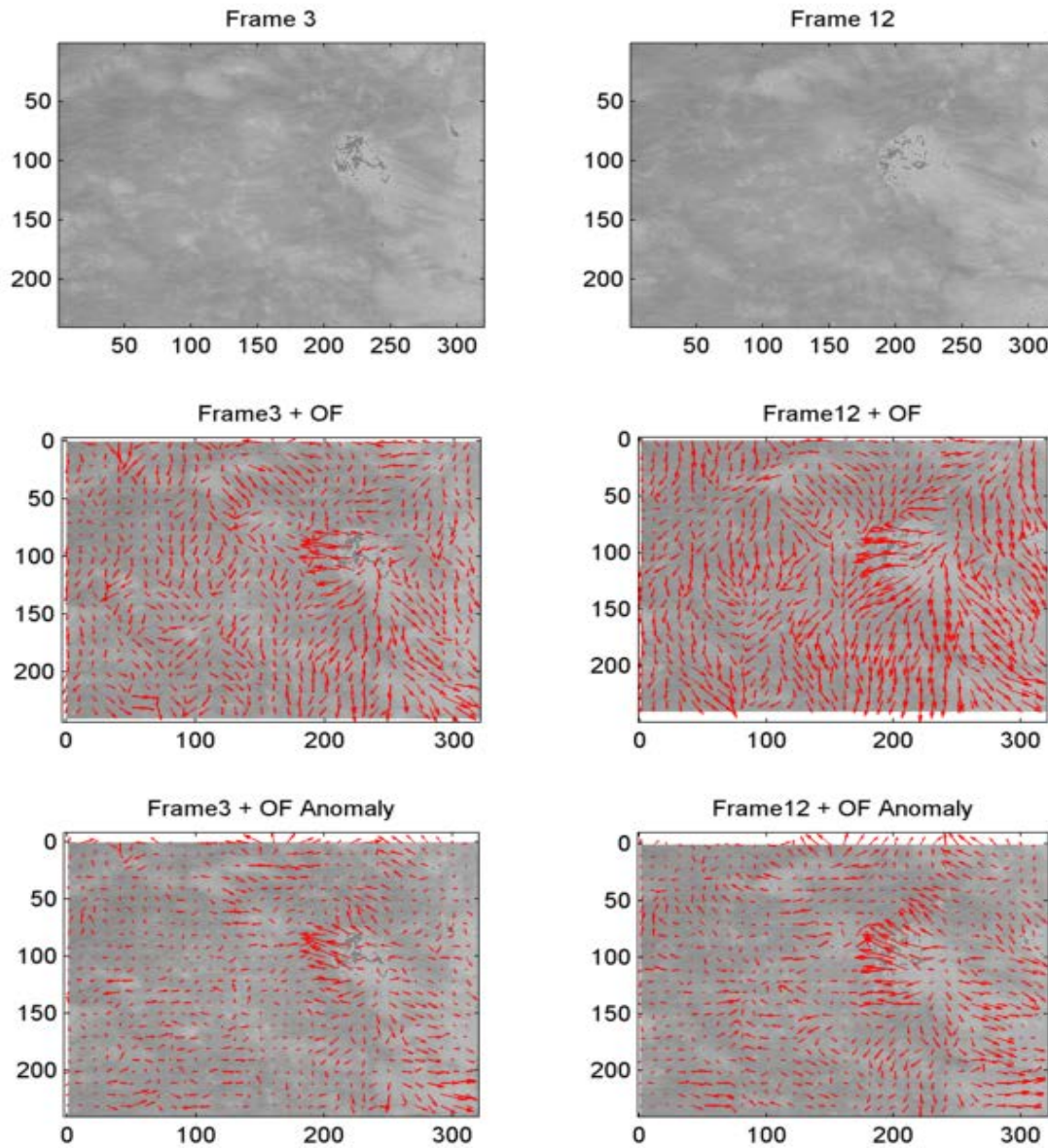


Figure 13- Figure 12- example of the OFderived velocity field for two frames 3/20s apart during run 1.

The advective surface approach is based on *Dugan and Piotowski (2012)* who showed how to determine the surface flow magnitude and direction by fitting the 2D planar surface which arises from advective variance detectable in 3D spectra of airborne visible imagery. Computing 3D spectra of the first 3000 frames of each run, we clearly see the advective signal as depicted in Figure 15b. For less than 3000 frames, the advective signal is not usually as clearly visible. We perform a linear least square fit of the advective surface in wavenumber frequency slices of the 3D spectra at various angles relative to the image. The slope of the linear fit is the magnitude of the advection at that angle. Fitting a sinusoidal to the obtained magnitudes as a function of angle, as illustrated in Figure 15b, we determine the magnitude and direction of the surface flow as the maximum of the fit and the corresponding angle.

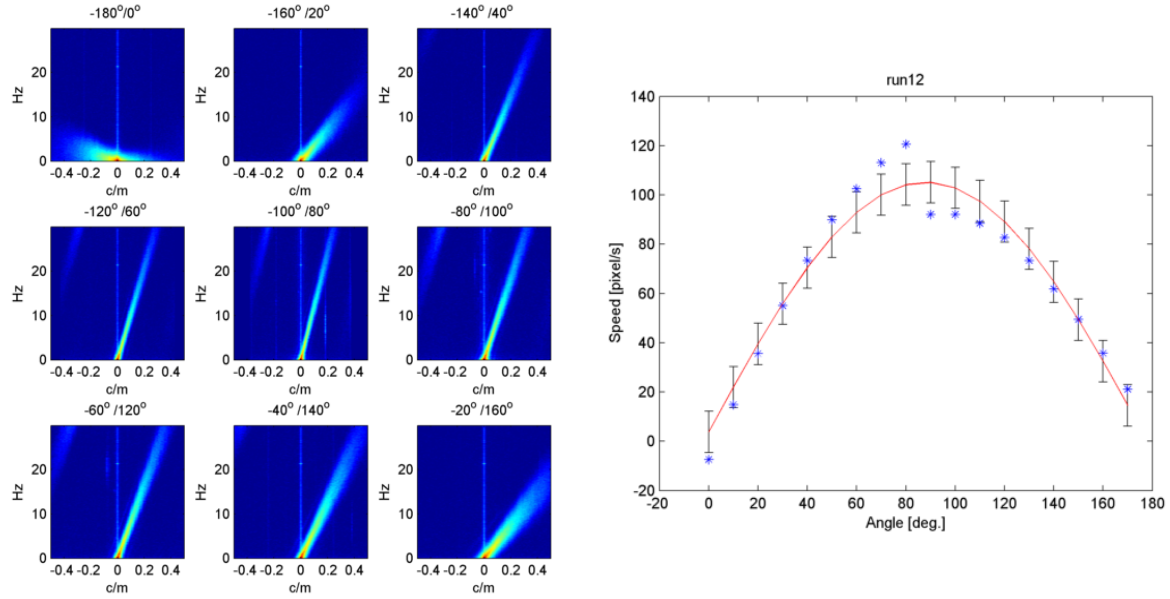


Figure 15- left: slices at different angles through the 3D spectra of run 12 clearly displaying and advective surface; right: sinusoidal fitted to the slopes of the advective surface.

Figure 16 shows the magnitude of the mean flow over 3000 frames for all runs obtained by the OF against that obtained from the PIV and SAS method. The correlation coefficient is $R=0.90$ for PIV vs. OF magnitudes. For mean flows of under 40 pixel/s the OF and PIV magnitudes are almost on the 1:1 line, however, for stronger flows the PIV gives surface current magnitudes up to 60 pixels/sec higher than the OF. The advective surface method gives higher velocities than both the PIV and the OF. The correlation coefficient is $R=0.96$ between the advective surface method and the PIV method and $R=0.86$ between the advective surface method and the OF method.

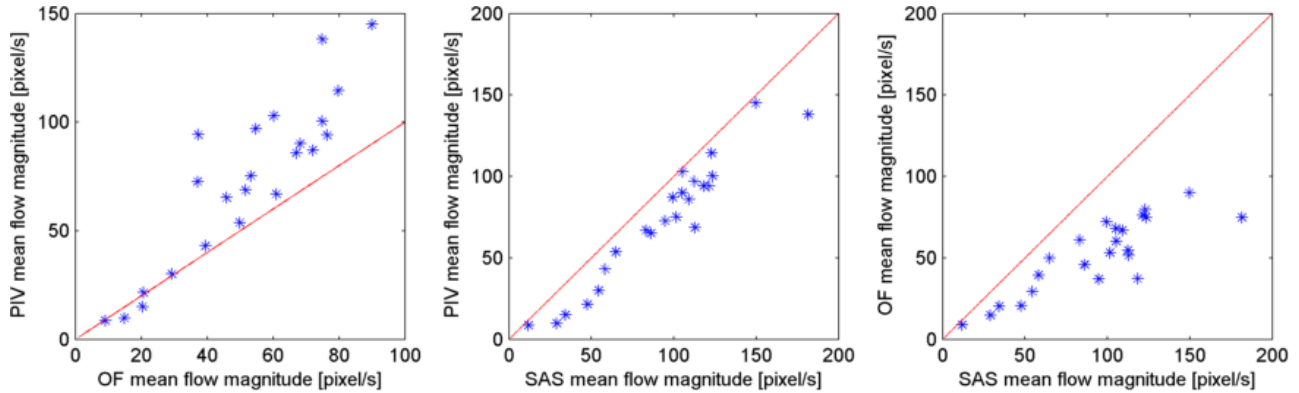


Figure 16- scatter plots of the run mean velocity magnitudes over 3000 frames derived from the PIV method vs. the OF method, PIV vs. SAS and OF vs. SAS. In red the 1:1 line.

Comparing the magnitudes of the velocities derived from the Skin temperature with the 3 different methods to those measured by the ADV, we see good agreement between the measured and the IR derived velocities; the latter being slightly weaker than the former (c.f. Figures 17 and 18). The correlation between the derived and measured velocity magnitudes are high: $R = 0.88$ for PIV, $R = 0.80$ for OF and $R = 0.92$ for SAS.

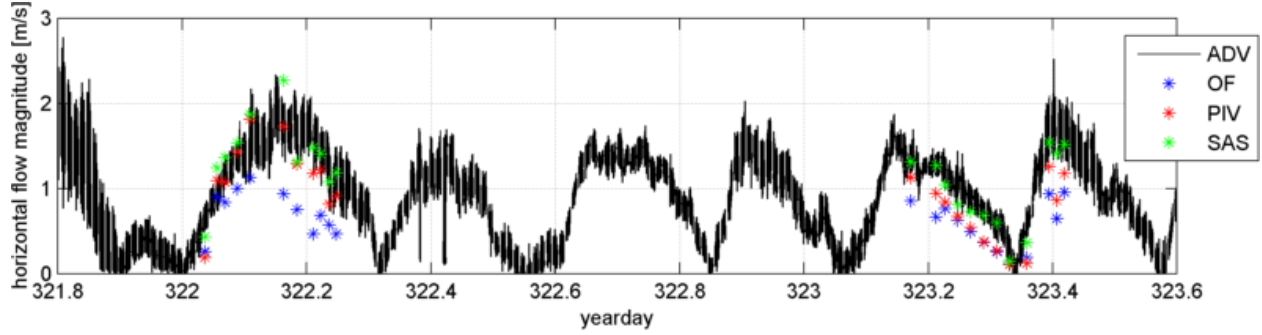


Figure 17. Time series of the flow magnitude measured by the ADV 11m above the river floor. The coloured stars represent the run mean flow magnitudes obtained by the 3 methods: PIV, OF and SAS.

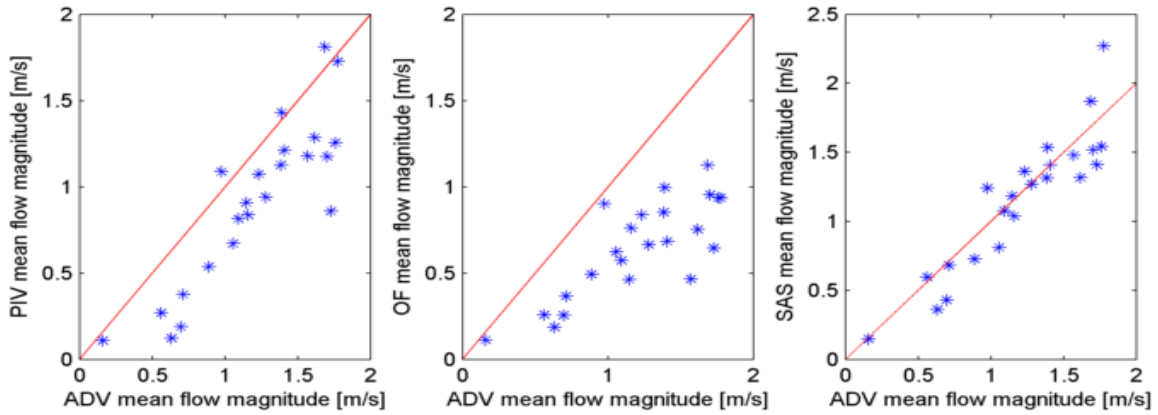


Figure 18- scatter plots of the run mean velocity magnitude over ~1 minute derived from the PIV method vs. measured ADV velocity magnitude, OF vs. ADV and SAS vs. ADV. In red the 1:1 line.

Filtering of Reflection in IR imagery

In order to remove the reflection seen in certain IR images, our ongoing efforts also evaluate different filtering techniques. As mentioned above, when reflectance is visible, one can detect underlying skin temperature patterns which are advected by the flow and an overlaying “film” of reflectance which is not always moving in the same direction as the flow. This incite us to use a filtering approach in which only the advective signal seen in the 3DFFT is kept and filter out all other signals to reconstruct an image where only the thermal structures and no reflectance are present.

IMPACT/APPLICATIONS

Although in this field campaign the IR remote sensing was performed from a ship, the analysis and results obtained in this study should be easily adaptable to imagery taken from other platforms such as aircrafts, manned and unmanned, as well as fixed platforms. The empirical relationships will allow inferring subsurface flow characteristics via non-intrusive monitoring which should permit monitoring over larger, not necessarily easily accessible areas.

REFERENCES

- Brumley, B. H., and G. H. Jirka (1988), Air-water transfer of slightly soluble gases: Turbulence, interfacial processes and conceptual models, *PhysicoChemical Hydrodynamics*, 10(3), 295-319.
- Dugan, J.P. and C.C. Piotrowski (2012), Measuring currents in a coastal inlet by advection of turbulent eddies in airborne optical imagery, *Journal of Geophysical Research*, 117, C03020, 15 PP., doi:10.1029/2011JC007600
- McKenna, S. P., and W. R. McGillis (2004), The role of free-surface turbulence and surfactants in air-water gas transfer, *International Journal of Heat and Mass Transfer*, 47, 539-553.
- Garbe, C. S., H. Spies, and B. Jahne (2003), Estimation of surface flow and net heat flux from infrared image sequences, *Journal of Mathematical Imaging and Vision*, 19(3), 159-174.